3D homogenised strength criterion for masonry: application to drystone retaining walls

Le, HH, Garnier, D, Colas, A-S, Terrade, B & Morel, J-C

Original citation & hyperlink:
Le, HH, Garnier, D, Colas, A-S, Terrade, B & Morel, J-C 2016, '3D homogenised strength criterion for masonry: application to drystone retaining walls' Journal of the Mechanics and Physics of Solids, vol 95, pp. 239-253.
https://dx.doi.org/10.1016/j.jmps.2016.05.021

DOI 10.1016/j.jmps.2016.05.021
ISSN 0022-5096

Publisher: Elsevier

3D homogenised strength criterion for masonry: application to drystone retaining walls

Hong Hanh Le[a,1], Denis Garnier[b], Anne-Sophie Colas[c,*], Benjamin Terrade[c], Jean-Claude Morel[a]

[a] *Université de Lyon, Laboratoire Génie Civil et Bâtiment, LTDS (UMR 5513), ENTPE, 3 rue Maurice Audin, 69518 Vaulx-en-Velin, France.*
[b] *Université Paris-Est, Laboratoire Navier (UMR 8205), ENPC, IFSTTAR, CNRS, 6-8 avenue Blaise Pascal, 77455 Marne-la-Vallée, France.*
[c] *Université Paris-Est, MAST, SDOA, IFSTTAR, 14-20 boulevard Newton, 77447 Marne-la-Vallée, France.*

Abstract

A 3D strength criterion for masonry is constructed based on yield design theory. Yield design homogenisation provides a rigorous theoretical framework to determine the yield strength properties of a periodic medium, based on the properties of its constituent materials. First, theoretical basis of 2D homogenisation of periodic media, and more particularly its application in the framework of yield design, will be retrieved. Then, 2D principles are extended to exhibit a 3D domain of running-bond masonry. This criterion is finally used to assess the stability of a drystone retaining wall loaded by an axle load, and theoretical results are compared to experimental data. Perspectives on this work are given as a conclusion.

Keywords: masonry, homogenisation, strength criterion, drystone, retaining wall

*Corresponding author
[1] Present address: Faculty of Civil Engineering, National University of Civil Engineering, 59 Giai Phong Street, Hanoi, Vietnam.

1. Introduction

Structural analysis of historical constructions has received a growing attention over the past decades, due to the necessary preservation of its heritage. Actually, the development of modelling proves challenging, considering the strong heterogeneity of the masonry and the diversity of its constitutive materials and patterns.

Considering the relative periodicity of their pattern, masonry can be treated as periodic composite media, and homogenisation techniques can be applied in order to derive its mechanical characteristics at macro-scale from the properties of its constituent materials. Pande et al. (1989) pioneered this technique on masonry, in order to evaluate its equivalent modulus of elasticity. This work has been extended later on by Anthoine (1995), on a 3D finite thickness pattern. Homogenisation techniques have then been extensively used to assess elastic properties (Cecchi and K., 2002; Cecchi and Sab, 2002; Mistler et al., 2007), or in the framework of limit analysis (Milani et al., 2006a,b; Milani, 2008; Milani and Lourenço, 2010) and finite element analysis (Zucchini and Lourenço, 2002, 2004, 2009).

In 1997, de Buhan and de Felice propose an homogenisation approach for masonry developed in the framework of yield design theory. Yield design homogenisation is a rigorous theoretical approach to determine the yield strength properties of a periodic medium, based on the properties of its constituent materials. Extending on this work, the present article introduces a 3D macroscopic strength criterion for running-bond masonry, derived from the strength characteristics of blocks and joints.

First, theoretical basis of 2D homogenisation of periodic media, and more particularly its application in the framework of yield design, will be retrieved. This theory is then extended to the three-dimensional case, in order to exhibit a 3D macroscopic strength domain of running-bond masonry. An application of this work is finally given: the 3D strength criterion is used to assess the stability of drystone retaining wall loaded by an axle load in the framework of yield design, and theoretical results given by the model are compared to experimental data. Perspectives on this work are given as a conclusion.

2. Presentation of 2D homogenisation of periodic media principles

Homogenisation of period media consists in replacing the heterogeneous periodic medium by an equivalent homogeneous medium, which macroscopic mechanical properties are derived from the microscopic properties of the original heterogeneous medium. Introduced by Suquet (1983) in the framework of limit analysis, homogenisation technique has been extended on for yield design analysis of reinforced soils (de Buhan and Salençon, 1990), fibre composite materials (de Buhan and Taliercio, 1991), jointed rock mass (Bekaert and Maghous, 1996), and also masonry (de Buhan and de Felice, 1997).

Considering a heterogeneous periodic medium, a basic cell V can be identified as the smallest representative volume of material. For every point $\underline{x}$ of V, a microscopic strength domain $G(\underline{x})$ can be defined as the set of admissible stress fields $\underline{\underline{\sigma}}(\underline{x})$. Yield design homogenisation aims at defining the macroscopic strength domain G^{hom} of an equivalent homogeneous medium.

2.1. *Static definition of G^{hom}*

A static definition of the macroscopic strength domain G^{hom} can be given as the set of admissible macroscopic stress fields $\underline{\underline{\Sigma}}$:

$$G^{\text{hom}} = \left\{ \begin{array}{ll} \underline{\underline{\Sigma}} = \left\langle \underline{\underline{\sigma}}(\underline{x}) \right\rangle = \dfrac{1}{V} \displaystyle\int_V \underline{\underline{\sigma}}(\underline{x}) \; \mathrm{d}V & \text{(1a)} \\ \underline{\operatorname{div}} \; \underline{\underline{\sigma}}(\underline{x}) = \underline{0} & \text{(1b)} \\ \underline{\underline{\sigma}}(\underline{x}).\underline{n}(\underline{x}) \text{ antiperiodic } (\underline{n} \text{ unit normal oriented outward}) & \text{(1c)} \\ \underline{\underline{\sigma}}(\underline{x}) \in G(\underline{x}) \quad \forall \, \underline{x} \in V & \text{(1d)} \end{array} \right\}$$

2.2. *Kinematic definition of G^{hom}*

A kinematic definition of the macroscopic strength domain G^{hom} can be given as the set of admissible macroscopic stress fields $\underline{\underline{\Sigma}}$:

$$G^{\text{hom}} = \left\{ \underline{\underline{\Sigma}} \; / \underline{\underline{\Sigma}} : \underline{\underline{D}} \leq \pi^{\text{hom}}(\underline{\underline{D}}) \right\} \tag{2}$$

where:

- $\underline{\underline{\Sigma}}$ is defined in equation (1a);
- $\underline{\underline{D}}$ is the macroscopic strain rate field given by :

$$\underline{\underline{D}} = \langle \underline{\underline{d}}(\underline{x}) \rangle = \frac{1}{2\,V} \int_V \left(\underline{\underline{\operatorname{grad}}} \, \underline{v}(\underline{x}) + {}^t \, \underline{\underline{\operatorname{grad}}} \, \underline{v}(\underline{x}) \right) \; \mathrm{d}V \tag{3}$$

- $\pi^{\text{hom}}(\underline{\underline{D}})$ is the support function of G^{hom} defined as:

$$\pi^{\text{hom}}(\underline{\underline{D}}) = \sup_{\underline{\underline{\Sigma}}} \left\{ \underline{\underline{\Sigma}} : \underline{\underline{D}} / \underline{\underline{\Sigma}} \in G^{\text{hom}} \right\} \tag{4}$$

Considering the periodicity of the medium, the virtual velocity field $\underline{v}(\underline{x})$ is given by:

$$\underline{v}(\underline{x}) = \underline{\underline{F}} \, . \, \underline{x} + \underline{u}(\underline{x}) \tag{5}$$

where $\underline{\underline{F}}$ is a second order tensor and $\underline{u}(\underline{x})$ a periodic velocity field. The associated strain rate field $\underline{\underline{d}}$ can thus be written :

$$\underline{\underline{d}} = \underline{\underline{D}} + \underline{\underline{\delta}} \tag{6}$$

where $\underline{\underline{D}}$ is the symmetric part of $\underline{\underline{F}}$ and $\underline{\underline{\delta}}$ the strain rate field associated with $\underline{u}$.

De Buhan and de Felice (1997) assumed that the support function $\pi^{\text{hom}}(\underline{\underline{D}})$ of the macroscopic strength domain G^{hom} can be written depending on the support function $\pi(\underline{\underline{d}})$ of the microscopic strength domain $G(\underline{x})$:

$$\pi^{\text{hom}}(\underline{\underline{D}}) = \min_{\underline{v}} \langle \pi(\underline{\underline{d}}) \rangle \tag{7}$$

2.3. 2D homogenised strength criterion for masonry

The kinematic approach has been used by de Buhan and de Felice (1997) to determine a strength criterion G^{hom} for running-bond masonry. Masonry is made of blocks of height a and thickness b, linked by a joint considered infinitely thin. The basic cell chosen here has a diamond shape (Fig. 1), made of four pieces of blocks linked by three sections of joint.

Block strength properties are considered to be infinite, compared to the shear strength of the joints. The joints comply with a Mohr-Coulomb strength criterion:

$$g(\sigma, \tau) = |\tau| + \sigma \, \tan\varphi - c \leq 0 \tag{8}$$

where σ, τ are the normal and shear stress in the joints, φ the friction angle, and c the cohesion of the joints.

This criterion can also be expressed as a support function of the strength

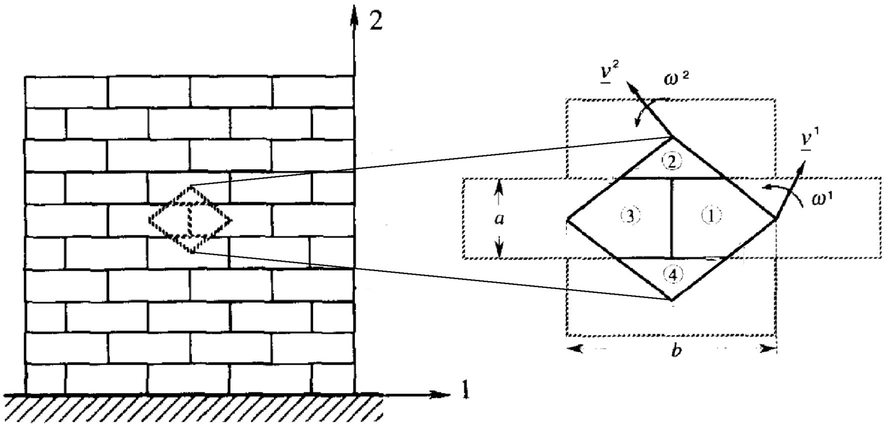

Figure 1: Periodic masonry in 2D, basic cell and rigid block velocity field by de Buhan and de Felice (1997).

domain (Salençon, 2013):

$$\pi(\underline{n}, \llbracket \underline{v} \rrbracket) = \begin{cases} \dfrac{c}{\tan\varphi} \llbracket \underline{v} \rrbracket.\underline{n} & \text{if } \llbracket \underline{v} \rrbracket.\underline{n} \geq |\llbracket \underline{v} \rrbracket| \sin\varphi \\ \infty & \text{otherwise} \end{cases} \tag{9}$$

The hypothesis of an infinite compressive strength implies that the support function $\pi(\underline{\underline{d}})$ takes infinite values for $\underline{\underline{d}} \neq \underline{\underline{0}}$, implying:

$$\underline{\underline{d}} = \underline{\underline{0}} \tag{10}$$

Thus, the only relevant velocity fields are rigid body fields, which can be written as:

$$\underline{v}(x) = \underline{v}^i + \omega^i \underline{e}_3 \wedge (\underline{x} - \underline{x}^i) \tag{11}$$

where $\underline{v}^i$ is the translation velocity, ω^i the angular velocity, and $\underline{x}^i$ the position of a point in the block i ($i = 1 \ldots 4$).

Indeed, Bekaert and Maghous (1996) showed that periodicity conditions imposes $\omega^i = 0$. The velocity fields thus reduce to translations, that can be written as:

$$\underline{v}^1 = -\underline{v}^3 = \underline{\alpha} \tag{12a}$$

$$\underline{v}^2 = -\underline{v}^4 = \underline{\beta} \tag{12b}$$

With these velocity fields (12), equation (5) enables the calculation of $\underline{\underline{F}}$:

$$\underline{\underline{F}} = \frac{2}{b}\,\underline{\alpha} \otimes \underline{e}_1 + \frac{1}{a}\,\underline{\beta} \otimes \underline{e}_2 \tag{13}$$

and equation (6) the calculation of $\underline{\underline{D}}$:

$$\underline{\underline{D}} = \frac{1}{b}\,\underline{\alpha} \otimes^s \underline{e}_1 + \frac{1}{2a}\underline{\beta} \otimes^s \underline{e}_2 \tag{14}$$

where $\underline{u} \otimes^s \underline{v} = \frac{1}{2}\left(\underline{u} \otimes \underline{v} + \underline{v} \otimes \underline{u}\right)$

Yet, the maximum resisting work $\langle\pi(\underline{\underline{d}})\rangle$ in the basic cell is given by:

$$\left\langle\pi(\underline{\underline{d}})\right\rangle = \frac{1}{V}\left(\int_V \pi(\underline{\underline{d}})\,\mathrm{d}V + \int_S \pi(\underline{n}, [\![\,\underline{v}\,]\!]\,)\,\mathrm{d}S\right) \tag{15}$$

Considering (10) and (9), this expression can be simplified to:

$$\left\langle\pi(\underline{\underline{d}})\right\rangle = \frac{c}{\tan\varphi}\left(\frac{2}{b}\alpha_1 + \frac{1}{a}\beta_2\right) \tag{16}$$

De Buhan and de Felice (1997) prove that, combining (7), (14) and (16), the expression of the support function $\pi^{\mathrm{hom}}(\underline{\underline{D}})$ is finally given by:

$$\pi^{\mathrm{hom}}(\underline{\underline{D}}) = \langle\pi(\underline{\underline{d}})\rangle = \frac{c}{\tan\varphi}\,\mathrm{tr}\left(\underline{\underline{D}}\right) \tag{17}$$

provided the relevancy conditions:

$$-D_{11} \leq 0 \tag{18a}$$

$$f\,D_{11} \leq 2m\,D_{22} \tag{18b}$$

$$2\,|D_{12}| \leq f\,D_{11} + \frac{1}{f}\,D_{22} \quad \text{if } 2m < \frac{1}{f} \tag{18c}$$

where $f = \tan\varphi$, and $m = a/b$ is the aspect ratio of the blocks.

The macroscopic strength domain G^{hom} is thus given by:

$$G^{\text{hom}} = \left\{ \underline{\underline{\Sigma}} \,/ \underline{\underline{\Sigma}} : \underline{\underline{D}} \leq \pi^{\text{hom}}(\underline{\underline{D}}) = \frac{c}{\tan\varphi}\,\text{tr}\left(\underline{\underline{D}}\right) \right\} \tag{19}$$

Fig. 2 shows the representation of G^{hom} in the space of stresses. This representation exhibits the anisotropic character of the masonry.

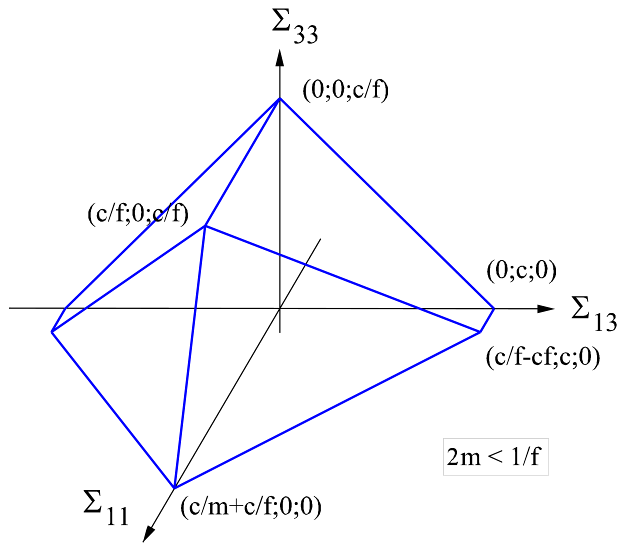

Figure 2: Macroscopic strength domain G^{hom} for running-bond masonry.

3. Generalisation to 3D homogenised strength criterion for masonry

The 2D plane strain approach is here extended on to 3D modelisation. The wall is now considered to be made of blocks of width a, thickness b, and height c, arranged with running bond in the plane of the wall and stack bond out-of-plane (Fig. 3). This pattern has been chosen because it enables an analytical resolution of the problem.

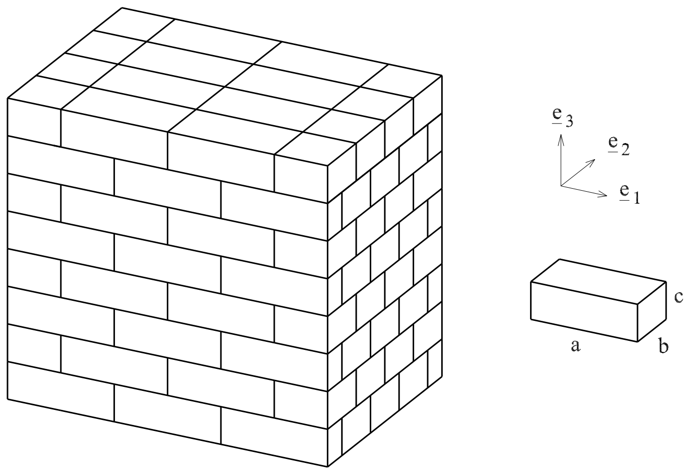

Figure 3: Periodic masonry in 3D.

The basic cell is a vertical prism (Fig. 4), made of 13 pieces of blocks. It consists in 3 beds of masonry, and presents a diamond-shape cross-section in the plane $(\underline{e}_1, \underline{e}_2)$ along beds direction. Indeed, the basic cell is perfectly symmetric around its centre.

Block compressive strength is still considered to be infinite, with zero-thickness joints complying with a Mohr-Coulomb strength criterion. The hypothesis of an infinite compressive strength still implies equation (10). Thus, the only relevant velocity fields are still rigid body fields.

Complying with equation (5) and periodicity conditions, the following expressions can be written:

$$\underline{v}_1 - \underline{v}_2 \quad = \quad \underline{\underline{F}} \,.\, (2a\,\underline{e}_1) \qquad \text{(20a)}$$

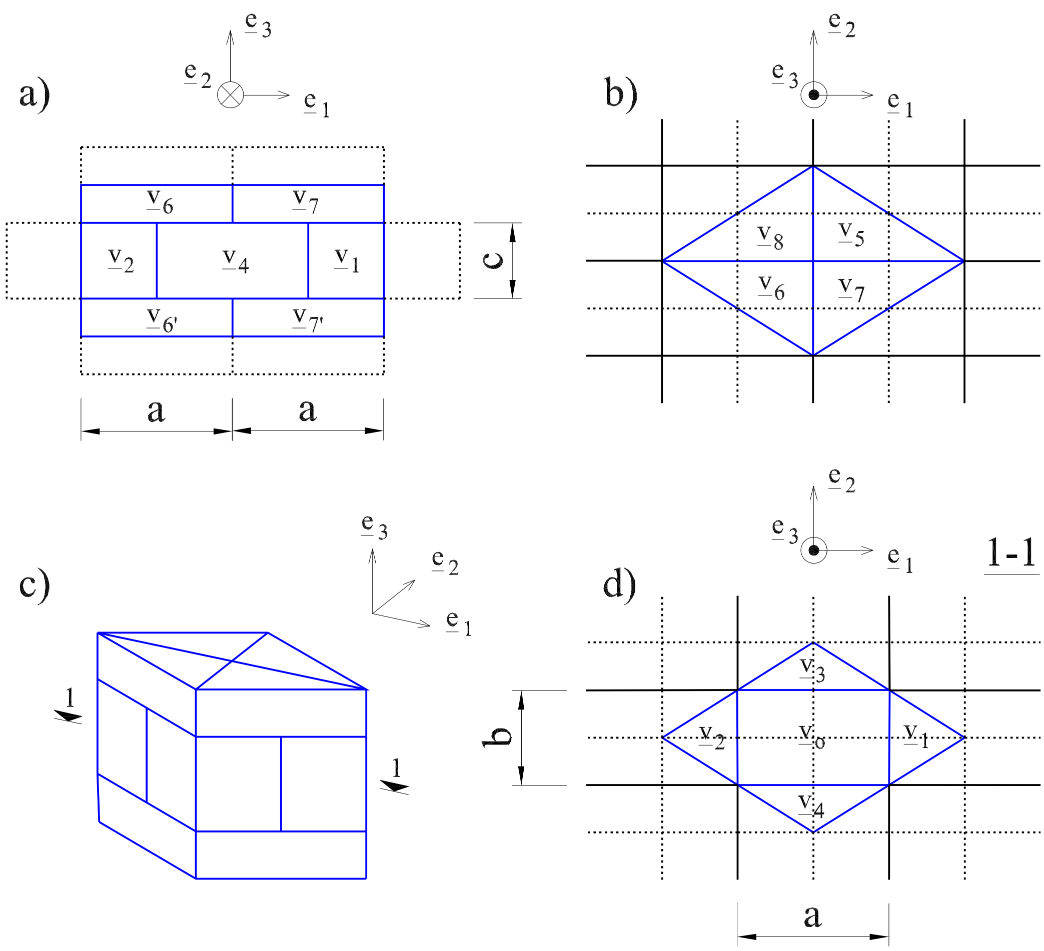

Figure 4: 3D basic cell of masonry.

$$\begin{aligned}
\underline{v}_3 - \underline{v}_4 &= \underline{\underline{F}} \,.\, (2b\, \underline{e}_2) && (20b)\\
\underline{v}_5 - \underline{v}_{5'} = \underline{v}_6 - \underline{v}_{6'} = \underline{v}_7 - \underline{v}_{7'} = \underline{v}_8 - \underline{v}_{8'} &= \underline{\underline{F}} \,.\, (2c\, \underline{e}_3) && (20c)\\
\underline{v}_1 - \underline{v}_4 = \underline{v}_3 - \underline{v}_2 = \underline{v}_5 - \underline{v}_6 = \underline{v}_{5'} + \underline{v}_{6'} &= \underline{\underline{F}} \,.\, (a\, \underline{e}_1 + b\, \underline{e}_2) && (20d)\\
\underline{v}_7 - \underline{v}_8 = \underline{v}_{7'} + \underline{v}_{8'} = \underline{v}_1 - \underline{v}_3 = \underline{v}_4 - \underline{v}_2 &= \underline{\underline{F}} \,.\, (a\, \underline{e}_1 + b\, \underline{e}_2) && (20e)
\end{aligned}$$

Assuming the velocity of block 0 is null, the following notations can thus be introduced:

$$\underline{v}_0 = \underline{0} \tag{21a}$$

$$\underline{v}_2 = -\underline{v}_1 = -\underline{\alpha} \tag{21b}$$

$$\underline{v}_4 = \underline{v}_3 = -\underline{\beta} \tag{21c}$$

$$\underline{v}_{5'} = -\underline{v}_6 = -\underline{\varepsilon} + \frac{1}{2}\left(\underline{\alpha} + \underline{\beta}\right) \tag{21d}$$

$$\underline{v}_{6'} = -\underline{v}_5 = -\underline{\varepsilon} - \frac{1}{2}\left(\underline{\alpha} + \underline{\beta}\right) \tag{21e}$$

$$\underline{v}_{7'} = -\underline{v}_8 = -\underline{\varepsilon} + \frac{1}{2}\left(\underline{\alpha} - \underline{\beta}\right) \tag{21f}$$

$$\underline{v}_{8'} = -\underline{v}_7 = -\underline{\varepsilon} - \frac{1}{2}\left(\underline{\alpha} - \underline{\beta}\right) \tag{21g}$$

With these velocity fields (21), equation (5) enables the calculation of $\underline{\underline{F}}$:

$$\underline{\underline{F}} = \frac{1}{a}\,\underline{\alpha} \otimes \underline{e}_1 + \frac{1}{b}\,\underline{\beta} \otimes \underline{e}_2 + \frac{1}{c}\,\underline{\varepsilon} \otimes \underline{e}_3 \tag{22}$$

and the symmetric part of $\underline{\underline{F}}$, represented by the matrix $\underline{\underline{\tilde{D}}}$ in the base $(\underline{e}_1, \underline{e}_2, \underline{e}_3)$:

$$\underline{\underline{\tilde{D}}} = \begin{bmatrix} \dfrac{\alpha_1}{a} & \dfrac{1}{2}\left(\dfrac{\alpha_2}{a} + \dfrac{\beta_1}{b}\right) & \dfrac{1}{2}\left(\dfrac{\alpha_3}{a} + \dfrac{\varepsilon_1}{c}\right) \\ \dfrac{1}{2}\left(\dfrac{\alpha_2}{a} + \dfrac{\beta_1}{b}\right) & \dfrac{\beta_2}{b} & \dfrac{1}{2}\left(\dfrac{\beta_3}{b} + \dfrac{\varepsilon_2}{c}\right) \\ \dfrac{1}{2}\left(\dfrac{\alpha_3}{a} + \dfrac{\varepsilon_1}{c}\right) & \dfrac{1}{2}\left(\dfrac{\beta_3}{b} + \dfrac{\varepsilon_2}{c}\right) & \dfrac{\varepsilon_3}{c} \end{bmatrix}_{(\underline{e}_1, \underline{e}_2, \underline{e}_3)} \tag{23}$$

Yet, the maximum resisting work $\langle \pi(\underline{\underline{d}}) \rangle$ in the basic cell is given by:

$$\left\langle \pi(\underline{\underline{d}}) \right\rangle = \frac{1}{V}\left(\int_V \pi(\underline{\underline{d}})\, \mathrm{d}V + \int_J \pi(\underline{n}, [\![\, \underline{v} \,]\!])\, \mathrm{d}J \right) = \frac{c}{\tan\phi}\left(\frac{\alpha_1}{a} + \frac{\beta_2}{b} + \frac{\varepsilon_3}{c} \right) \tag{24}$$

The support function $\pi^{\text{hom}}(\underline{\underline{D}})$ is finally given by (17):

$$\pi^{\text{hom}}(\underline{\underline{D}}) = \frac{c}{\tan\varphi}\,\text{tr}(\underline{\underline{D}})$$

provided the relevancy conditions:

$$\begin{aligned}
\underline{\alpha}\,.\,\underline{e}_1 &\geq |\underline{\alpha}|\,\sin\varphi && \text{(25a)}\\
\underline{\beta}\,.\,\underline{e}_2 &\geq |\underline{\beta}|\,\sin\varphi && \text{(25b)}\\
(\underline{\varepsilon}+\frac{1}{2}(\underline{\alpha}+\underline{\beta}))\,.\,\underline{e}_3 &\geq |\underline{\varepsilon}+\frac{1}{2}(\underline{\alpha}+\underline{\beta})|\,\sin\varphi && \text{(25c)}\\
(\underline{\varepsilon}-\frac{1}{2}(\underline{\alpha}+\underline{\beta}))\,.\,\underline{e}_3 &\geq |\underline{\varepsilon}-\frac{1}{2}(\underline{\alpha}+\underline{\beta})|\,\sin\varphi && \text{(25d)}\\
(\underline{\varepsilon}+\frac{1}{2}(\underline{\alpha}-\underline{\beta}))\,.\,\underline{e}_3 &\geq |\underline{\varepsilon}+\frac{1}{2}(\underline{\alpha}-\underline{\beta})|\,\sin\varphi && \text{(25e)}\\
(\underline{\varepsilon}-\frac{1}{2}(\underline{\alpha}-\underline{\beta}))\,.\,\underline{e}_3 &\geq |\underline{\varepsilon}-\frac{1}{2}(\underline{\alpha}-\underline{\beta})|\,\sin\varphi && \text{(25f)}
\end{aligned}$$

The macroscopic strength domain G^{hom} is still given by equation (2).

It is interesting to note that, considering plane strain conditions, the same results as those given by de Buhan and de Felice (1997) are achieved. In particular, the macroscopic deformation rate (23) becomes:

$$\underline{\underline{\tilde{D}}} = \begin{bmatrix} \dfrac{\alpha_1}{a} & 0 & \dfrac{1}{2}\left(\dfrac{\alpha_3}{a}+\dfrac{\varepsilon_1}{c}\right) \\ 0 & 0 & 0 \\ \dfrac{1}{2}\left(\dfrac{\alpha_3}{a}+\dfrac{\varepsilon_1}{c}\right) & 0 & \dfrac{\varepsilon_3}{c} \end{bmatrix}_{(\underline{e}_1,\underline{e}_2,\underline{e}_3)} \qquad (26)$$

that is plane strain expression recorded in (14). Indeed, G^{hom} is represented by Fig. 2 for plane strain conditions in $(\underline{e}_1,\, \underline{e}_3)$.

4. Application to the stability assessment of drystone retaining walls

The three-dimensional strength criterion identified in section 3 is now used to assess the stability of a drystone retaining wall.

Drystone walling is an ancient, vernacular form of construction that can be found in many areas around the world. In western Europe, drystone accounts for a large part of the retaining walls along road networks. Despite the robustness of these structures, drystone walls are subjected to deterioration due to ageing, excessive loading for which they were not designed, or even inappropriate repairs, and there is a growing need for structural analysis methods in order to evaluate their residual bearing capacity. Over the past two decades, advances have been made in France and in the UK for modelling the plane strain behaviour of drystone earth retaining walls. The distinct element method has been extensively used for modelling drystone retaining wall behaviour, more precisely for a better understanding of their pathologies due to ageing (Harkness et al., 2000; Powrie et al., 2002; Claxton et al., 2005; Walker et al., 2007). On the other hand, limit equilibrium analyses have been applied to assess the ultimate bearing capacities of these structures (Villemus et al., 2007; Mundell et al., 2009). More recently, this approach has been extended on, using the rigorous framework of yield design (Colas et al., 2010a, 2013). Along with these simulation developments, full-scale experimental campaigns have been undertaken in plane strain (Villemus et al., 2007; Colas et al., 2010b), and 3D (Mundell et al., 2010; McCombie et al., 2012), in order to calibrate and validate the models.

Relying on this work, the present paper proposes an innovative 3D modelling of these structures. Actually, retaining walls comply with a plane strain behaviour when they only support their backfill soil but when considering a traffic loading upon the backfill, a three-dimensional approach should be adopted. The effects of traffic loadings can be represented by a point load $\underline{F}$ applied on a rigid plate situated upon the backfill, at a distance d of the head of the wall, to figure the action of an axle. This study aims to assess the ultimate load $\underline{F}^+$ the wall can bear, solely knowing the geometry of the structure, the loading mode and the strength criterion of the constituent materials.

4.1. Statement of the hypotheses

The stability assessment is undertaken in the framework of yield design theory: the first step consists in identifying the inputs of the model, being the geometry, loading mode and material strength criterion of the structure. The geometry and the loading mode are easily described by Fig. 5 and 6. The strength criteria are detailed below.

Strength criterion of the wall. The macroscopic strength criterion constructed in section 3 can be used to characterise drystone, provided the cohesion of the joints is set to 0. The friction angle φ now represents the friction angle between the blocks. Expression (2) thus becomes:

$$G^{\text{hom}} = \left\{ \underline{\underline{\Sigma}} \,/ \underline{\underline{\Sigma}} : \underline{\underline{D}} \leq \pi^{\text{hom}}(\underline{\underline{D}}) = 0 \right\} \tag{27}$$

and the homogenised support function $\pi^{\text{hom}}(\underline{\underline{D}})$:

$$\pi^{\text{hom}}(\underline{\underline{D}}) = 0 \tag{28}$$

with respect to the relevancy conditions given by (25).

Strength criterion of the soil. The backfill soil has been considered as a purely frictional Mohr-Coulomb soil, where φ_s is the friction angle of the soil. Cohesion of the soil has been considered as null to simplify calculations and for safety reasons.

The support function and the relevancy conditions of the soil can be found in Salençon (2013):

$$\pi\left(\underline{\underline{d}}_s\right) = 0 \text{ provided } \operatorname{tr} \underline{\underline{d}}_s \geq (|d_{s1}| + |d_{s2}| + |d_{s3}|) \sin \varphi_s \tag{29}$$

$$\pi\left(\underline{n}_s, [\![\, \underline{v}_s \,]\!]\right) = 0 \text{ provided } [\![\, \underline{v}_s \,]\!] \,.\, \underline{n}_s \geq |[\![\, \underline{v}_s \,]\!]| \sin \varphi_s \tag{30}$$

where d_{si} are the eigenvalues of the strain rate $\underline{\underline{d}}_s$, and $[\![\, \underline{v}_s \,]\!]$ the velocity discontinuity across a discontinuity surface of normal $\underline{n}_s$.

Strength criterion at the soil/structure interaction. The interface has been considered as a purely frictional Mohr-Coulomb interface, where δ the friction of the interface equals φ_s the friction angle of the soil. This choice is motivated by the rough nature of the drystone upstream face, which can force the failure to occur into the backfill.

The support function and the relevancy conditions of the interface can be found in Salençon (2013):

$$\pi\left(\underline{n}_\delta, \underline{\Delta v}\right) = 0 \text{ provided } \underline{\Delta v} \,.\, \underline{n}_\delta \geq |\underline{\Delta v} \,.\, \underline{t}_\delta| \tan \delta \tag{31}$$

where $\underline{\Delta v}$ is the velocity discontinuity at the interface, $\underline{n}_\delta$ the normal and $\underline{t}_\delta$ the tangent of the discontinuity surface.

Tab. 1 gathers the input parameters of the yield design model.

Table 1: Input parameters of the 3D drystone retaining wall models.

	Symbol	Unit	Definition
Geometry	H	m	Wall height
	l	m	Wall thickess at the top
	f_1	%	Wall batter
	d	m	Distance axle load/top of the wall
	B	m	Half width of the plate
Loading	$\underline{\gamma}$	kN/m^3	Wall unit weight
	$\underline{\gamma_s}$	kN/m^3	Backfill unit weight
	$\underline{F}$	kN	Axle load
Strength	φ	°	Block friction angle
	φ_s	°	Soil internal friction angle

4.2. Construction of the virtual velocity fields

Fig. 5 and 6 show the velocity field family chosen for this study: it consists in a translation of a part of the backfill and a translation of part of the wall. It presents a plane of symmetry (O, $\underline{e}_1$, $\underline{e}_3$). Considering the complexity of the calculations, it has been decided to restrain to plane failure surfaces.

4.2.1. Velocity field within the wall.

The wall is supposed to fail into 2 parts: a failure zone (JRSTJ'R'S'T'), which is given a translation velocity $\underline{v}$, whereas the rest of the wall remains motionless. The failure zone is delimited by a horizontal surface (JJ'T'T) at the bottom and two quadrilateral shapes (JRST) and (J'R'S'T') on the

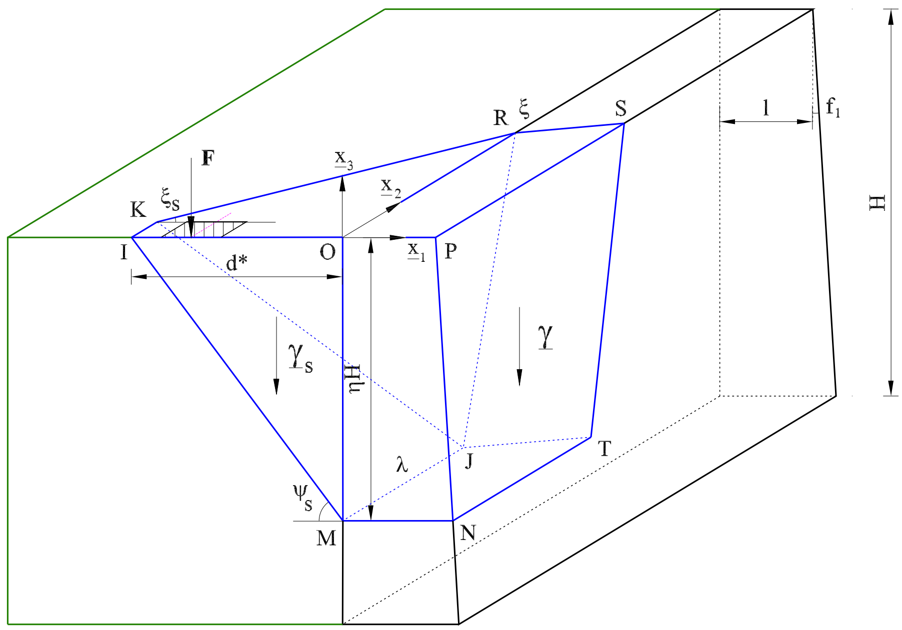

Figure 5: Yield design analysis of a drystone retaining wall subjected to a single axle load: geometry, loading, and velocity fields on a half-system cross-section.

edges. The failure zone is bounded by its height ηH, with $\eta \in [0,1]$, and the angles ξ and χ respectively between (JRST) or (J'R'S'T') and the axis $\underline{e}_1$ and $\underline{e}_3$. The surface (JJ'T'T) is taken horizontal because it is the optimal solution available with analytical calculations.

The virtual translation velocity $\underline{v}$ of part (JRSTJ'R'S'T') is written:

$$\underline{v} = V\ \cos\theta\,\underline{e}_1 + V\ \sin\theta\,\underline{e}_3 \tag{32}$$

where θ is the angle between $\underline{v}$ and $\underline{e}_1$.

This velocity fields has to comply with the relevancy conditions (25) imposed by the masonry strength criterion.

Failure surface (JTT'J'). Considering the macroscopic parameters, the strain rate $\underline{\underline{D}}$ is given by:

$$\underline{\underline{D}} = \underline{n} \otimes^s [\![\underline{v}]\!] \tag{33}$$

where $\underline{v}$ is given by (32) and $\underline{n} = \underline{e}_3$.

Thus:

$$\tilde{\underline{\underline{D}}} = \begin{bmatrix} 0 & 0 & \dfrac{V}{2}\cos\theta \\ 0 & 0 & 0 \\ \dfrac{V}{2}\cos\theta & 0 & V\sin\theta \end{bmatrix}_{(\underline{e}_1,\underline{e}_2,\underline{e}_3)} \tag{34}$$

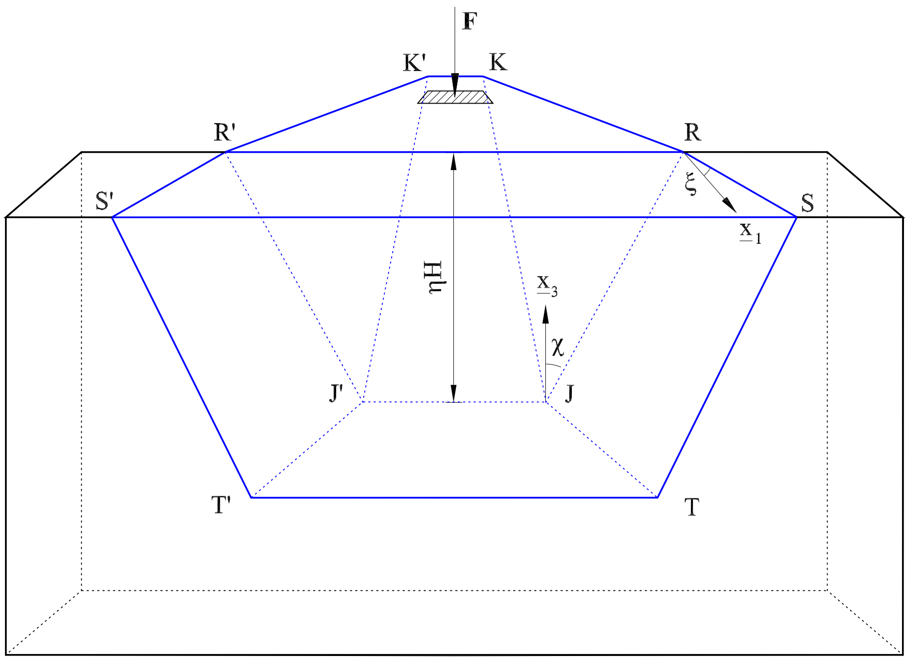

Figure 6: Yield design analysis of a drystone retaining wall subjected to a single axle load: geometry, loading, and velocity fields on a front view.

Yet, $\underline{\underline{D}}$ is also given by (23), using microscopic parameters. Based on (34) and (23), microscopic and macroscopic parameters are thus easily identified:

$$\begin{aligned}
\underline{\alpha} &= \underline{\beta} = \underline{0} && (35a)\\
\varepsilon_1 &= cV\,\cos\theta && (35b)\\
\varepsilon_2 &= 0 && (35c)\\
\varepsilon_3 &= cV\,\sin\theta && (35d)
\end{aligned}$$

Relevancy conditions are finally given by substituting expression given by (35) in (25):

$$\theta \geq \varphi \tag{36}$$

Failure surfaces (JRST) and (J'R'S'T'). Considering the symmetry of the structure, the calculations will be developed on surface (JRST) only, the expressions for (J'R'S'T') being easily derived.

The strain rate $\underline{\underline{D}}$ is still given by (33), with $\underline{v}$ given by (32) and $\underline{n}$ by:

$$\underline{n} = \frac{\tan\xi\,\underline{e_1} - \underline{e_2} + \tan\chi\,\underline{e_3}}{\sqrt{\tan^2\xi + 1 + \tan^2\chi}} \tag{37}$$

Thus:

$$\underline{\underline{\tilde{D}}} = \begin{bmatrix} \dfrac{V\tan\xi\cos\theta}{\sqrt{\tan^2\xi+1+\tan^2\chi}} & -\dfrac{V\cos\theta}{2\sqrt{\tan^2\xi+1+\tan^2\chi}} & \dfrac{V\left(\tan\chi\,\cos\theta+\tan\xi\,\sin\theta\right)}{2\sqrt{\tan^2\xi+1+\tan^2\chi}} \\ -\dfrac{V\cos\theta}{2\sqrt{\tan^2\xi+1+\tan^2\chi}} & 0 & -\dfrac{V\sin\theta}{2\sqrt{\tan^2\xi+1+\tan^2\chi}} \\ \dfrac{V\left(\tan\chi\,\cos\theta+\tan\xi\,\sin\theta\right)}{2\sqrt{\tan^2\xi+1+\tan^2\chi}} & -\dfrac{V\sin\theta}{2\sqrt{\tan^2\xi+1+\tan^2\chi}} & \dfrac{V\,\tan\chi\sin\theta}{\sqrt{\tan^2\xi+1+\tan^2\chi}} \end{bmatrix} \tag{38}$$

Based on the macroscopic (38) and the microscopic (23) definitions of $\underline{\underline{\tilde{D}}}$, microscopic and macroscopic parameters are thus easily identified:

$$\beta_1 = \beta_2 = \beta_3 = 0 \tag{39a}$$

$$\alpha_1 = \frac{aV \tan\xi \cos\theta}{\sqrt{\tan^2\xi + 1 + \tan^2\chi}} \tag{39b}$$

$$\alpha_2 = -\frac{aV \cos\theta}{\sqrt{\tan^2\xi + 1 + \tan^2\chi}} \tag{39c}$$

$$\varepsilon_2 = -\frac{cV \sin\theta}{\sqrt{\tan^2\xi + 1 + \tan^2\chi}} \tag{39d}$$

$$\varepsilon_3 = \frac{cV \tan\chi \sin\theta}{\sqrt{\tan^2\xi + 1 + \tan^2\chi}} \tag{39e}$$

$$\frac{\alpha_3}{a} + \frac{\varepsilon_1}{c} = \frac{V(\tan\chi \cos\theta + \tan\xi \sin\theta)}{\sqrt{\tan^2\xi + 1 + \tan^2\chi}} \tag{39f}$$

In order to get analytical solutions, the following choices have been made:

$$\alpha_3 = aV \frac{\tan\chi \cos\theta}{\sqrt{\tan^2\xi + 1 + \tan^2\chi}} \tag{40a}$$

$$\varepsilon_1 = cV \frac{\tan\xi \sin\theta}{\sqrt{\tan^2\xi + 1 + \tan^2\chi}} \tag{40b}$$

Relevancy conditions are finally given by substituting expression given by (39) and (40) in (25):

$$\left\{ \begin{array}{rcl} \varphi & \leq & \pi/4 \\ \tan\theta & \geq & a/(2\,c) \\ \chi & = & \xi \\ \tan\xi & \geq & \tan\varphi/\sqrt{1-\tan^2\varphi} \end{array} \right. \tag{41}$$

Calculations are detailed in Appendix A.

4.2.2. Velocity field within the soil

The backfill soil is supposed to fail into two parts: a failure zone (KRJJ'R'K'), which is given a translation velocity $\underline{v}_s$, whereas the rest of the backfill remains motionless. The failure zones of the wall and the backfill intersect in the vertical plane formed by the upper face of the wall, quoted (JRR'J'). The plane (KJJ'K') forms an angle Ψ_s with $\underline{e}_1$, defined by:

$$\tan\Psi_s = \frac{\eta\, H}{d^*} \tan\Psi_s = \frac{\eta\, H}{d^*} \tag{42}$$

where d^* is the distance between (KK') and (RR').

The virtual translation velocity $\underline{v}_s$ of part (KRJJ'R'K') is written:

$$\underline{v}_s = V_s\, \cos(\psi_s - \varphi_s)\, \underline{e}_1 - V_s\, \sin(\psi_s - \varphi_s)\, \underline{e}_3 \tag{43}$$

Considering the velocity field chosen in (43), there is no deformation in the backfill, thus $\underline{\underline{d}}_s = \underline{\underline{0}}$ and $\pi(\underline{\underline{d}}_s) = 0$. The maximum resisting work of the backfill is solely governed by the support function (30), provided the relevancy condition is satisfied. On (KJJ'K'), the condition is fulfilled as the angle with $\underline{v}_s$ is equal to φ_s. On surface (KRJ), the normal $\underline{n}_s$ is given by:

$$\underline{n}_s = \frac{\tan\xi_s\, \underline{e}_1 - \underline{e}_2 + \tan\chi\, \underline{e}_3}{\sqrt{\tan^2\xi_s + 1 + \tan^2\chi}} \tag{44}$$

with $\tan\xi_s = (\lambda + \eta\, H\, \tan\chi - B)/d^*$.

The relevancy condition becomes:

$$\frac{\cos(\psi_s - \varphi_s)\, \tan\xi_s - \sin(\psi_s - \varphi_s)\, \tan\chi}{\sqrt{\tan^2\xi_s + 1 + \tan^2\chi}} \geq \sin\varphi_s \tag{45}$$

4.2.3. Velocity jump at the soil/structure interface

At the soil/structure interface, the support function is given by (31) and the relevancy condition becomes:

$$V \geq V_s\, \frac{\cos(\psi_s - 2\,\varphi_s)}{\cos(\theta + \varphi_s)} \tag{46}$$

4.3. Upper bound axle load

The kinematic approach of yield design is based on the application of the principle of virtual works:

$$\forall\, \underline{v} \text{ kinematically admissible, } W^{\mathrm{e}} \;\leq\; W^{\mathrm{mr}} \tag{47}$$

which provides an upper bound of the ultimate load $\underline{F}^{+}$.

Considering the support function of the wall (28), the soil (30), and the interface (31), the maximum resisting work W^{mr} is given by:

$$W^{\mathrm{mr}} = W^{\mathrm{mr}}_{\mathrm{wall}} + W^{\mathrm{mr}}_{\mathrm{soil}} + W^{\mathrm{mr}}_{\mathrm{interface}} = 0 \tag{48}$$

The work of the external forces W^e is given by the sum of the work of the forces in the wall, the soil and due to the axle load F:

$$W^{\mathrm{e}} = W^{\mathrm{e}}_{\mathrm{wall}} + W^{\mathrm{e}}_{\mathrm{soil}} + W^{\mathrm{e}}_{F} \tag{49}$$

The work of the external forces in the wall $W^{\mathrm{e}}_{\mathrm{wall}}$ is written:

$$\begin{aligned} W^{\mathrm{e}}_{\mathrm{wall}} &= \int_V \underline{\gamma} \,.\, \underline{v}\; \mathrm{d}V \\ W^{\mathrm{e}}_{\mathrm{wall}} &= -\gamma\, V\, \sin\theta \left[\frac{\eta H}{2}\,(l + \frac{\eta H}{2}\, f_1)(2\lambda + 2\eta H \tan\chi + 2l\tan\xi + \eta H f_1 \tan\xi)\right] \end{aligned} \tag{50}$$

The work of the external forces in the soil $W^{\mathrm{e}}_{\mathrm{soil}}$ is written:

$$\begin{aligned} W^{\mathrm{e}}_{\mathrm{soil}} &= \int_V \underline{\gamma}_s \,.\, \underline{v}_s\; \mathrm{d}V \\ W^{\mathrm{e}}_{\mathrm{soil}} &= \gamma_s\, V_s\, \sin(\psi_s - \varphi_s) \left[B\, d^*\, \eta\, H + \frac{1}{3}\, d^*\, \eta\, H\, (\lambda - B + \eta\, H\, \tan\chi)\right] \end{aligned} \tag{51}$$

The work of the external forces due to the axle load W^{e}_{F} is written:

$$W^{\mathrm{e}}_{F} = \underline{F} \,.\, \underline{v}_F = F\, V_s\, \sin(\psi_s - \varphi_s) \tag{52}$$

The upper bound inequality (47) leads to:

$$F \leq -\frac{W^{\mathrm{e}}_{\mathrm{wall}} + W^{\mathrm{e}}_{\mathrm{soil}}}{V_s \sin(\psi_s - \varphi_s)} = f\left(\eta, d^*, \chi, \xi, \lambda, \theta\right) \qquad \forall\, \eta, d^*, \chi, \xi, \lambda, \theta \tag{53}$$

The analytical solution of the upper-bound load F^+ is written depending on input parameters of the problem (H, l, f_1, d, B, γ, φ, γ_s, φ_s) and kinematic parameters (η, d^*, χ, ξ, λ, θ). The upper bound load F^+ is finally given by minimizing function f:

$$F^+ = \min_{\eta, d^*, \chi, \xi, \lambda, \theta} f\left(\eta, d^*, \chi, \xi, \lambda, \theta\right) \tag{54}$$

with respect to the relevancy conditions (41), (45), and (46)

5. Comparison with full-scale experiments

The analytical approach performed in section 4 is tested by comparison with experimental results by Mundell et al. (2010) and McCombie et al. (2012). Actually, between 2004 and 2009, the University of Bath has undertaken full-scale experiments on drystone retaining walls, aiming at better understanding the three-dimensional behaviour of these structures, and more particularly the bulge deformation of existing drystone walls. Five experimental drystone walls were built on a moving platform, backfilled by crushed gravel, raised to ensure full frictional interface between the wall and the backfill, and finally loaded by a localised surcharge upon the backfill surface, except for wall 1 which was also submitted to tilting of the platform. Wall 1 was built according to standards of drystone construction, whereas walls 2 to 5 were intentionally of poorer construction quality to ensure bulge deformations and failures. Considering the difference of construction and testing protocol of the first test, it has been decided to focus on walls 2 to 5 in this study. Geometrical and physical characteristics of the walls, as well as experimental results are given in Tab. 2.

(a) (b)

Figure 7: Experimental tests at the University of Bath (Mundell et al., 2010; McCombie et al., 2012): experimental wall (a) and axle load over the backfill (b).

Considering the specific experimental protocol, with the moving platform, and the poor quality of construction of the walls, the experimental campaign cannot be used directly to validate the model. Yet, it provides a practical framework for a parametric analysis. Thus, the yield design approach previously developed is used to estimate an upper-bound of the ultimate axle load the experimental walls can bear, then compared to the experimental value. The preliminary question which has to be faced with is the choice of the input parameters of the model, and more particularly the aspect ratio of the blocks. Actually, as drystone masonry is made of uncut blocks of different

Table 2: Experimental tests at the University of Bath (Mundell et al., 2010; McCombie et al., 2012): geometrical and physical characteristics, and experimental results.

	Wall 2	Wall 3	Wall 4	Wall 5
Type of stone	limestone	limestone	limestone	slate
Wall height (m)	2.5	2.5	2.5	2.5
Backfill height(m)	2.2	2.2	2.2	2.2
Wall top thickness (m)	0.3	0.4	0.4	0.4
Wall base thickness (m)	0.5	0.6	0.7	0.67
Wall batter (%)	0.08	0.08	0.12	0.11
Wall unit weight (kN/m^3)	19.9	16.8	17	19.7
Backfill unit weight (kN/m^3)	13.7	13.7	13.7	13.7
Block friction angle (°)	37.4	37.4	37.4	17.5
Backfill friction angle (°)	39	39	39	39
Distance load/wall (m)	1	1	1	1
Experimental load (kN)	75	80	85	60

size, it proves quite difficult to evaluate this parameter. Yet, aspect ratio is only involved in the calculation of θ, the angle of the translation velocity of the wall $\underline{v}$ with the horizontal $\underline{e}_1$, so that:

$$\theta = \max\left\{\arctan(a/2c), \varphi\right\} \tag{55}$$

The influence of this parameter is assessed on wall 5, as slate friction angle is quite low, compared to limestone friction angle. Fig. 8 shows the evolution of the analytical upper-bound load F^+ depending on the aspect ratio a/c. It can be seen that the analytical solution tends to the experimental value as a/c decreases, and even reaches it for $a/c \approx 0.6$. This value seems very low as the average aspect ratio of slate blocks seems greater than 2.

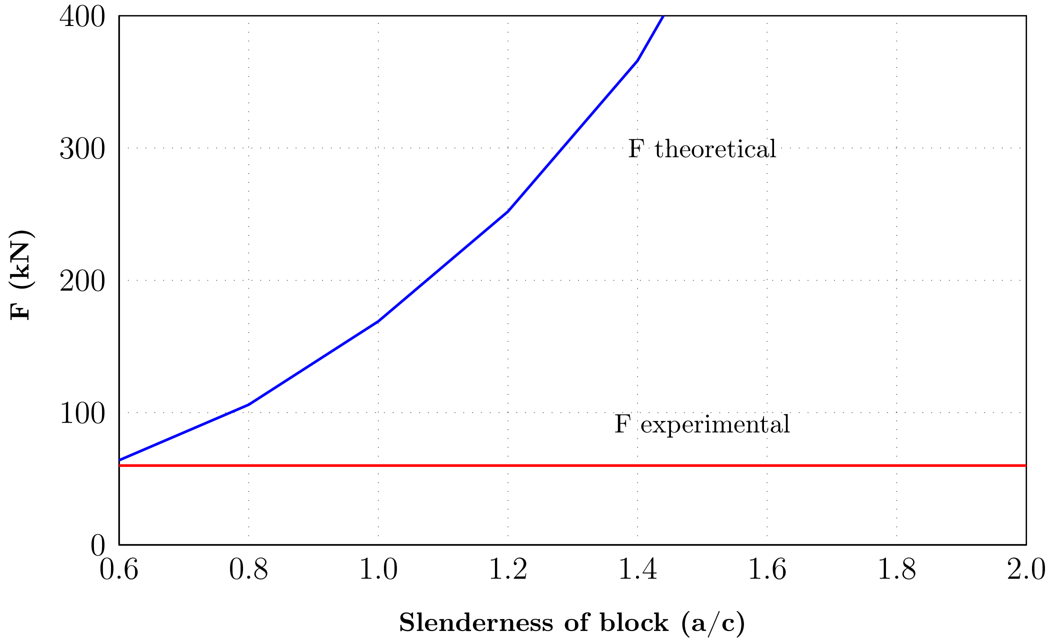

Figure 8: Comparison between theoretical and experimental ultimate load on experiments from the University of Bath, depending on the block aspect ratio a/c.

Comparing theoretical and experimental upper bound values for F (Fig. 9), it is worth noting that yield design kinematic approach overestimates the bearing capacities of drystone experimental walls, which is consistent with the poor quality of construction of the walls and the upper-bound approach of the model. With a aspect ratio $a/c = 1$, theoretical values are 6.5 times greater than experimental results for limestone walls. This can be accounted for by the relevancy conditions on the macroscopic strength criterion of masonry, which force the velocity field to form an angle $\theta \geq \varphi$. An additional possible explanation is the value of the friction angle considered in this study. Actually, the experimental campaign by Colas et al. (2010a) has showed that the bed joint friction angle in a drystone wall proves about 10° lower than the block friction angle measured in laboratory. This can be explained by the internal rotation of the blocks located at the basis of the wall, and by the difference of contact between wall bed joints and smooth block joints. Considering a lower friction angle between limestone blocks (27.4° instead of 37.4°), the difference between analytical and experimental solutions vanishes to 3, showing the great influence of block friction angle in the model.

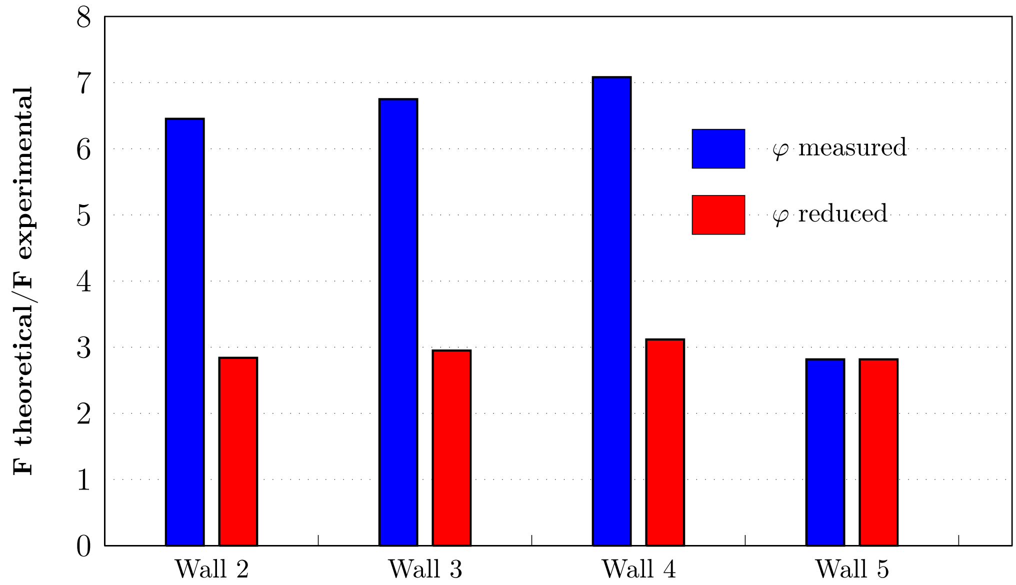

Figure 9: Comparison between theoretical and experimental ultimate load on experiments from the University of Bath (a/c=1)

The application of the model on an experimental campaign has highlighted the importance the block aspect ratio and the block friction angle on the results, thus enabling a qualitative evaluation of the model. Yet, the discrepancies between theoretical and experimental values prevent from a quantitative validation. A forthcoming experimental campaign is planned, with experimental walls according to standards of construction and a unique loading mode by a single axle load. This campaign aims to assess the model, and provides additional information on drystone wall 3D behaviour.

6. Conclusion

This paper presents a homogenised 3D strength criterion for masonry. The development of this criterion enables the design and the stability assessment of masonry structures in the framework of yield design. An application is here presented through the stability assessment of drystone retaining walls loaded by a single axle load. Yield design offers a simple but rigorous framework to perform a structural evaluation. Theoretical results are finally compared with experimental results found in the literature: this comparison proves the importance of the input parameters in the model, and more especially the block aspect ratio and the block friction angle. It also highlights the importance of complying experiments with modelling. Perspectives on this work includes greater account taken of the joint friction angle, by distinguishing horizontal and vertical joints. Scale down and full-scale experiments will also be planed in order to get experimental results dedicated to the model, thus enabling a better validation of theoretical results.

References

Anthoine, A., 1995. Derivation of the in-plane elastic characteristics of masonry through homogenization theory. Int J Solids Struct 32 (2), 137–163.

Bekaert, A., Maghous, S., 1996. Three-dimensional yield strength properties of jointed rock mass as a homogenized medium. Mechanics of Cohesive-frictional Materials 1 (1), 1–24.

Cecchi, A., K., S., 2002. A multi-parameter homogenization study for modeling elastic masonry. Eur J Mech A Solids 21, 249–268.

Cecchi, A., Sab, K., 2002. Out of plane model for heterogeneous periodic materials: the case of masonry. Eur J Mech A Solids 21 (5), 715–746.

Claxton, M., Hart, R. A., McCombie, P. F., Walker, P. J., 2005. Rigid block distinct-element modeling of dry-stone retaining walls in plane strain. J Geotech Geoenviron Eng 131 (3), 381–389.

Colas, A. S., Morel, J. C., Garnier, D., 2010a. 2D modelling of a dry joint masonry wall retaining a pulverulent backfill. Int J Numer Anal Methods Geomech 34 (12), 1237–1249.

Colas, A.-S., Morel, J.-C., Garnier, D., 2010b. Full-scale field trials to assess dry-stone retaining wall stability. Eng Struct 32 (5), 1215–1222.

Colas, A. S., Morel, J. C., Garnier, D., 2013. Assessing the two-dimensional behaviour of drystone retaining walls by full-scale experiments and yield design simulation. Géotechnique 63 (2), 107–117.

de Buhan, P., de Felice, G., 1997. A homogenization approach to the ultimate strength of brick masonry. J Mech Phys Solids 45 (7), 1085–1104.

de Buhan, P., Salençon, J., 1990. Yield strength of reinforced soils as anistropic media. In: Mechanical Engineering Publications. J. P. Boehler, pp. 791–803.

de Buhan, P., Taliercio, A., 1991. A homogenisation approach to the yield strength of composite materials. Eur J Mech A Solids 10 (2), 129–154.

Harkness, R., Powrie, W., Zhang, X., Brady, K., O'Reilly, M., 2000. Numerical modelling of full-scale tests on drystone masonry retaining walls. Géotechnique 50 (2), 165–179.

McCombie, P. F., Mundell, C., Heath, A., Walker, P., 2012. Drystone retaining walls: ductile engineering structures with tensile strength. Eng Struct 45, 238–243.

Milani, G., 2008. 3D upper bound limit analysis of multi-leaf masonry walls. Int J Mech Sci 50 (4), 817–836.

Milani, G., Lourenço, P. B., Tralli, A., 2006a. Homogenised limit analysis of masonry walls, part I: Failure surfaces. Comput Struct 84 (3-4), 166–180.

Milani, G., Lourenço, P. B., Tralli, A., 2006b. Homogenised limit analysis of masonry walls, part II: Structural examples. Comput Struct 84 (3-4), 181–195.

Milani, G., Lourenço, P. B., 2010. A simplified homogenized limit analysis model for randomly assembled blocks out-of-plane loaded. Comput Struct 88 (11-12), 690–717.

Mistler, M., Anthoine, A., Butenweg, C., 2007. In-plane and out-of-plane homogenisation of masonry. Comput Struct 85 (17-18), 1321–1330.

Mundell, C., McCombie, P., Bailey, C., Heath, A., Walker, P., 2009. Limit-equilibrium assessment of drystone retaining structures. Geotech Eng 162 (4), 203–212.

Mundell, C., McCombie, P. F., Heath, A., Harkness, J., Walker, P., 2010. Behaviour of drystone retaining structures. Struct Build 163 (1), 3–12.

Pande, G. N., Liang, J. X., Middleton, J., 1989. Equivalent elastic moduli for brick masonry. Comput Geotech 8, 243–265.

Powrie, W., Harkness, R., Zhang, X., Bush, D., 2002. Deformation and failure modes of drystone retaining walls. Géotechnique 52 (6), 435–446.

Salençon, J., 2013. Yield Design. Wiley-ISTE, London.

Suquet, P., 1983. Analyse limite et homogénéisation. C R Acad Sci 296, 1355–1358.

Villemus, B., Morel, J. C., Boutin, C., 2007. Experimental assessment of dry stone retaining wall stability on a rigid foundation. Eng Struct 29 (9), 2124–2132.

Walker, P., McCombie, P., Claxton, M., 2007. Plane strain numerical model for drystone retaining walls. Geotech Eng 160 (2), 97–103.

Zucchini, A., Lourenço, P. B., 2002. A micro-mechanical model for the homogenisation of masonry. Int J Solids Struct 39 (12), 3233–3255.

Zucchini, A., Lourenço, P. B., 2004. A coupled homogenisation-damage model for masonry cracking. Comput Struct 82 (11-12), 917–929.

Zucchini, A., Lourenço, P. B., 2009. A micro-mechanical homogenisation model for masonry: Application to shear walls. Int J Solids Struct 46 (3-4), 871–886.

AppendixA. Determination of the relevancy conditions for the velocity field within the wall

The appendix aims at detailing the calculation of relevancy conditions (41) of the velocity jump on surface (JRST) of the wall.

Based on the macroscopic (38) and the microscopic (23) definitions of $\underline{\underline{\tilde{D}}}$, microscopic and macroscopic parameters are thus easily identified:

$$\frac{V\ \tan\xi\ \cos\theta}{\sqrt{\tan^2\xi+1+\tan^2\chi}} = \frac{\alpha_1}{a} \tag{A.1a}$$

$$-\frac{V\ \cos\theta}{\sqrt{\tan^2\xi+1+\tan^2\chi}} = \frac{\alpha_2}{a}+\frac{\beta_1}{b} \tag{A.1b}$$

$$\frac{V\left(\tan\chi\ \cos\theta+\tan\xi\ \sin\theta\right)}{\sqrt{\tan^2\xi+1+\tan^2\chi}} = \frac{\alpha_3}{a}+\frac{\varepsilon_1}{c} \tag{A.1c}$$

$$0 = \frac{\beta_2}{b} \tag{A.1d}$$

$$-\frac{V\ \sin\theta}{\sqrt{\tan^2\xi+1+\tan^2\chi}} = \frac{\beta_3}{b}+\frac{\varepsilon_2}{c} \tag{A.1e}$$

$$\frac{V\ \tan\chi\ \sin\theta}{\sqrt{\tan^2\xi+1+\tan^2\chi}} = \frac{\varepsilon_3}{c} \tag{A.1f}$$

(A.1g)

β_1 and β_3 can be deduced from the introduction of condition (A.1d) in the microscopic relevancy condition (25b) :

$$\underline{\beta}\,.\,\underline{e}_2 = 0 \geq |\underline{\beta}|\ \sin\varphi \qquad \Rightarrow \qquad \beta_1=\beta_2=\beta_3=0 \tag{A.2}$$

The components of the velocity parameters can thus be identified (39):

$$
\begin{aligned}
\beta_1 &= \beta_2 = \beta_3 = 0 \\
\alpha_1 &= \frac{aV\ \tan\xi\ \cos\theta}{\sqrt{\tan^2\xi + 1 + \tan^2\chi}} \\
\alpha_2 &= -\frac{aV\ \cos\theta}{\sqrt{\tan^2\xi + 1 + \tan^2\chi}} \\
\varepsilon_2 &= -\frac{cV\ \sin\theta}{\sqrt{\tan^2\xi + 1 + \tan^2\chi}} \\
\varepsilon_3 &= \frac{cV\ \tan\chi\ \sin\theta}{\sqrt{\tan^2\xi + 1 + \tan^2\chi}} \\
\frac{\alpha_3}{a} + \frac{\varepsilon_1}{c} &= \frac{V(\tan\chi\ \cos\theta + \tan\xi\ \sin\theta)}{\sqrt{\tan^2\xi + 1 + \tan^2\chi}}
\end{aligned}
$$

In order to get analytical solutions, simplifying choices (40) have been made:

$$
\begin{aligned}
\alpha_3 &= aV\,\frac{\tan\chi\ \cos\theta}{\sqrt{\tan^2\xi + 1 + \tan^2\chi}} \\
\varepsilon_1 &= cV\,\frac{\tan\xi\ \sin\theta}{\sqrt{\tan^2\xi + 1 + \tan^2\chi}}
\end{aligned}
$$

Considering $\underline{\beta} = \underline{0}$ (A.2), the microscopic relevancy conditions vanish to:

$$
\begin{aligned}
\underline{\alpha} \,.\, \underline{e}_1 &\geq |\underline{\alpha}|\ \sin\varphi && \text{(A.3a)} \\
(\underline{\varepsilon} + \frac{1}{2}\,\underline{\alpha}) \,.\, \underline{e}_3 &\geq |\underline{\varepsilon} + \frac{1}{2}\,\underline{\alpha}|\ \sin\varphi && \text{(A.3b)} \\
(\underline{\varepsilon} - \frac{1}{2}\,\underline{\alpha}) \,.\, \underline{e}_3 &\geq |\underline{\varepsilon} - \frac{1}{2}\,\underline{\alpha}|\ \sin\varphi && \text{(A.3c)}
\end{aligned}
$$

Introducing components α_i and ε_i given by (39) and (40) in (A.3a) boils down to:

$$
\begin{aligned}
\alpha_1^2\ \cos^2\varphi &\geq (\alpha_2^2 + \alpha_3^2)\ \sin^2\varphi \qquad \text{(provided } \cos\theta > 0) \\
\tan^2\xi\ \cos^2\varphi &\geq (1 + \tan^2\chi)\ \sin^2\varphi \qquad\qquad \text{(A.4)} \\
\tan^2\xi &\geq (1 + \tan^2\chi)\ \tan^2\varphi
\end{aligned}
$$

Introducing components α_i and ε_i given by (39) and (40) in (A.3b) and (A.3c) boils down to:

$$\begin{aligned}
\left(\varepsilon_3 \pm \frac{\alpha_3}{2}\right)^2 \cos^2\varphi &\geq \left[\left(\varepsilon_1 \pm \frac{\alpha_1}{2}\right)^2 + \left(\varepsilon_2 \pm \frac{\alpha_2}{2}\right)^2\right] \sin^2\varphi \\
\tan^2\chi \left(c\,\sin\theta \pm \frac{a}{2}\cos\theta\right)^2 \cos^2\varphi &\geq \left[(1+\tan^2\xi)\,\left(c\,\sin\theta \pm \frac{a}{2}\cos\theta\right)^2\right] \sin^2\varphi \\
\tan^2\chi\,\cos^2\varphi &\geq (1+\tan^2\xi)\,\sin^2\varphi \qquad \left(\text{provided } c\,\sin\theta > \frac{a}{2}\cos\theta\right) \\
\tan^2\chi &\geq (1+\tan^2\xi)\,\tan^2\varphi
\end{aligned} \tag{A.5}$$

Combining expressions (A.4) and (A.5), the following conditions can be written:

$$\left\{\begin{aligned}
\tan\theta &\geq \frac{a}{2c} \\
\tan\chi = \tan\xi &\geq \frac{\tan\varphi}{\sqrt{1-\tan^2\varphi}} \\
\varphi &\leq \frac{\pi}{4}
\end{aligned}\right. \tag{A.6}$$

corresponding to the relevancy conditions given in (41).